Nanoplasmon-Nanoplasma Transition in Cu Nanoparticle: Distinction of Electron Emission

Xiang Huang, Hao Huang, Xu Han, Wei Cao, Qingbin Zhang,* and Peixiang Lu*

The electron response of nanoplasmon and nanoplasma in the laser field is greatly important for improving the functionality and efficiency of many potential applications. However, how and under what conditions the nanoplasmon-nanoplasma transition works remains poorly understood due to radiation damage and charge buildup. Utilizing the combined aerodynamic lens and velocity map imaging spectrometer, this transition mediated by different mechanisms are demonstrated, as verified by the distinct photoelectron momentum distributions from Cu nanoparticles. Initially the polarization-dependent distributions emphasize the domination of surface emission driven by the plasmonic field. Subsequently the transition starts and the competition of volume-multiphoton and thermionic emission plays the intermediate state dominating the transition process. Finally, a complete plasma is generated with the leading role of thermionic emission, which is confirmed by first observing the correlated electronic decay in metal nanoparticles. These findings bridge the gap between electron emission in nanoplasmonic and nanoplasma states and identify the mechanism-specific contributions, which will offer general principles for designing nanostructure and laser fields to control electron excitation and emission in practice.

1. Introduction

Nanostructured targets are of particular interest because they can improve laser energy coupling to the target at a microscopic spatial scale. The nanoscale energy localization introduces several unique, often exotic properties that do not persist in mesoscopic and macroscopic environments. These properties arise from the collective response of electrons driven by the laser field, which exists in two states: nanoplasmonic and nanoplasma states.[1–9] The difference is that in the nanoplasmonic state, the de-localized electrons oscillate around the ions firmly fixed to a crystalline lattice, whereas in the nanoplasma state, the lattice is completely destroyed.

These two electronic responses of nanotarget determine the efficiency and functionality of many applications. Plasmonic hot electrons are the heart of introducing nanometer site selectivity for the enhancements in catalytic activity.[10–13] Similar opportunities exist for solar energy conversion,[14,15] photodetection,[16,17] bright photocathodes,[18–20] terahertz nanoelectronics,[21] and femtosecond electron imaging.[22] The dilemma in these applications is to improve efficiency by increasing the laser intensity while avoiding the transition from plasmon to plasma. However, the requirement is different for the potential cancer nanomedicine application: nanoplasmonic and nanoplasma states should coexist.[23–27] The low-density plasma around the nanoparticle kills cancer cells, while the nanoparticle itself maintains a nanoplasmonic state to avoid the risk of toxicity issues induced by destruction.[28–31] In addition, nanoplasma devices, the nanoplasma-enabled picosecond switches[32] for example, normally necessitate a complete transition from plasmonic to the plasma state. The performance of such devices relies on the level of controlling the transition to nanoplasma.

Despite the crucial role in various nanoscale systems, how and what condition the nanoplasmon-nanoplasma transition works remains poorly understood. The difficulties stem from refreshing damaged nanoparticles and avoiding charge buildup while studying the transition.[33,34] Meanwhile, the electron yields of these two states differ by several orders of magnitude. The specific role of the co-existence of multiple ionization mechanisms is still confusing when the transition occurs.[35] There is a pressing need for new methods to investigate the nanoplasmon-nanoplasma transition.

This work distinguishes electron emission pathways during the nanoplasmon-nanoplasma transition in Cu nanoparticles (CuNPs). Experimentally we avoid radiation damage and charge buildup problems by constantly refreshing the samples with new ones utilizing the aerodynamic lens (ADL) system. The angle-resolved electron emission is recorded with yield across six orders of magnitude by operating the velocity map imaging (VMI) in either stacking or single-shot mode. In this case, we demonstrate

X. Huang, W. Cao, Q. Zhang, P. Lu
Wuhan National Laboratory for Optoelectronics and School of Physics
Huazhong University of Science and Technology
Wuhan 430074, China
E-mail: zhangqingbin@hust.edu.cn; lupeixiang@hust.edu.cn
H. Huang
School of Mechanical Science and Engineering
Huazhong University of Science and Technology
Wuhan 430074, China
X. Han, P. Lu
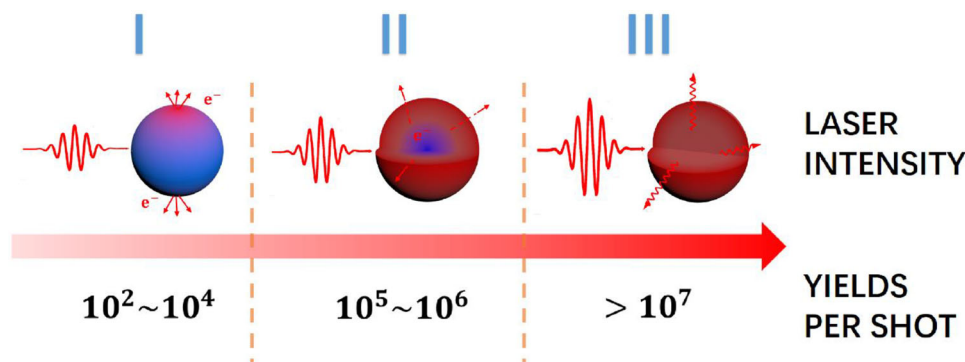Optics Valley Laboratory
Hubei 430074, China

Figure 1. Configuration of laser intensity correlated with electron yields per shot. The wide range of laser intensity is classified into three regions according to the feature of photoelectrons momentum distributions in the following discussion: In Region I, the red area shows dipole emission at the surface dominating the emission process. In Region II, the red color spreading into the particle indicates that photoemission occurs inside the particle. In Region III, the whole sphere turns red. The photoemission occurs across the whole nanoparticle as a result of thermionic emission.

the nanoplasmon-nanoplasma transition by the dramatically different photoelectron momentum distributions (PMDs) from the surface-multiphoton, volume-multiphoton, and thermionic emission, as reproduced by Monte Carlo modeling. Moreover, we present the first observation of correlated electronic decay (CED) in expanding solid nanoparticles and investigate the role of the space charge effect in metal-nanoplasma CED.

2. Results and Discussion

In our experiments, a nanoplasmon or nanoplasma is formed via the illumination of a CuNP (≈ 100 nm in diameter) with a tightly focused linear polarized laser pulse (≈ 35 fs, 800 nm). It is worth noting that the actual intensities irradiated on the CuNPs are sensitively dependent on their position within the laser focus because the sizes are much smaller than the focus volume. We thus employ a binning method to determine the local laser intensity for each CuNP. In this method, we get the histogram of the number of electrons emitted per laser shot and assume that the electron yields are directly correlated with the local laser intensity,[36,37] which is determined to fluctuate from 5×10^7 to 3.5×10^{13} Wcm^{-2} (see the Supporting Information). According to the characteristics of momentum distribution, we roughly divide the electron yields, or laser intensity, into three regions, as shown in the schematic in **Figure 1**.

We first analyzed the photoelectrons generated from CuNPs for Region I. For this low laser intensity, the photoelectron yields are too low to image a complete distribution in a single shot measurement, which requires at least 10^5 electron yields. Benefiting from the intensity "binning" method, we can select the measurements with similar electron yields to make a single-intensity approximation. And then, the selected measurements are added to generate a complete photoelectron distribution at this laser intensity. PMDs for the planes parallel (**Figure 2**a) and perpendicular (Figure 2b) to the laser polarization axis show distinctly different symmetries. The PMD for the plane perpendicular to the polarization is azimuthally isotropic, while another is notably anisotropic with stronger photoemission along the polarization axis, as shown by the angular distributions in Figure 2c. To quantify the anisotropy, the angular contrast, AC, is introduced

as AC $= \frac{\langle \perp \text{ yields} \rangle - \langle \parallel \text{ yields} \rangle}{\langle \perp \text{ yields} \rangle + \langle \parallel \text{ yields} \rangle}$, where the brackets denote averaging (within $\pm 1°$) over the orthogonal directions (90° and 270°) and parallel directions (0° and 180°) relative to the laser propagation axis. This definition of angular contrast provides a model-independent metric of anisotropy of PMD. In the plane parallel to polarization, the PMD shows a dipole-like character with AC = 0.133, indicating the stronger photoemission in the polarization direction. This is due to the formation of a polarization-depended enhancement field on the particle surface by the resonance of the dipolar excitations (see the Supporting Information). For comparison, the PMD perpendicular to the polarization is approximately isotropic with AC = 0.005. The fact that AC does not exactly equal zero can be attributed to the inhomogeneous responsivity of the imaging detector.

As the laser intensity increases into Region II in Figure 1, a single image can provide enough electrons to display all the distribution features. **Figure 3**a–c shows typical momentum spectra for three low to high laser intensities. Unlike the dipole-like character shown in Figure 2a, the low-energy electrons form an isotropic spot in the polarization plane. Besides, it is noticed that a symmetrical momentum ring appears abruptly at the periphery of the spot in Figure 3b,c. The isotropic nature of the observed central spot and the momentum ring (AC ≈ 0) strongly implies the transition from the polarization-dependent surface photoemission to a new emission mechanism.

To understand the origin of the central spot and the momentum ring, we trace their evolution as intensity increases. First, only the central spot appears without the momentum ring in Figure 3a, indicating that the spot appears at a lower intensity than the momentum ring. Second, although the central spot and the momentum ring both expand toward higher energy with increased laser intensity, the gap between the two differs in Figure 3b,c. To quantify the difference in these distributions, we depict the electron energy spectra in Figure 3e. In the spectra, the peak near zero kinetic energy corresponds to the central spot. After a fast decay, the energy spectrum corresponding to Figure 3a tends to flatten out, while the small hump is observed corresponding to the momentum ring in Figure 3b,c. By measuring the energy gap between the edge of the central spot and the momentum ring, we find that the energy interval decreases

**ADVANCED
SCIENCE NEWS**

www.advancedsciencenews.com

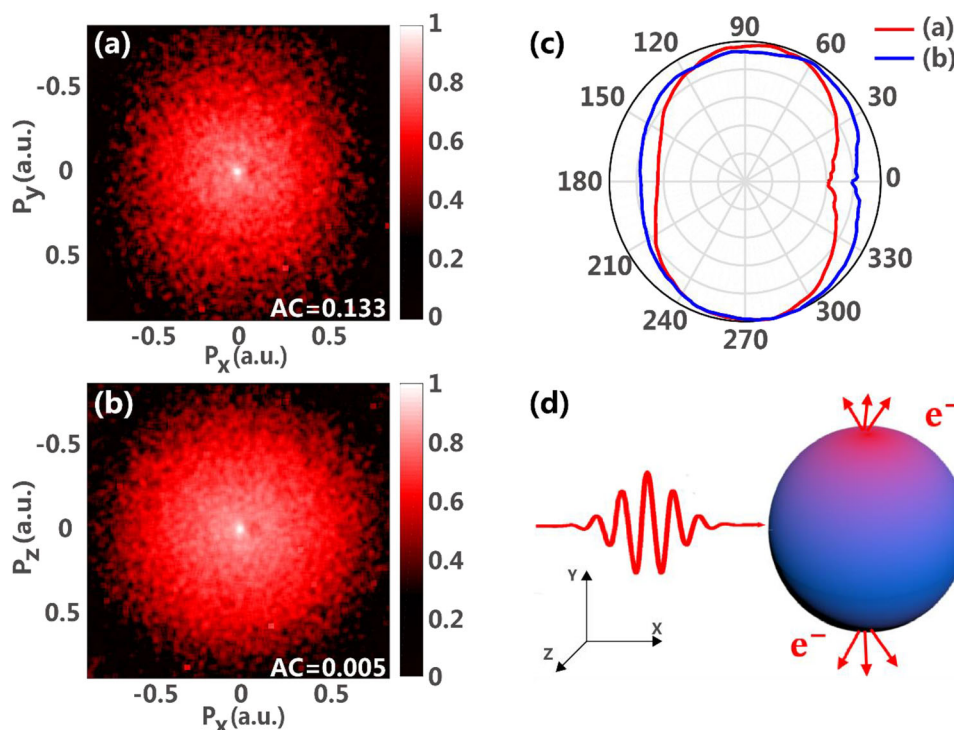LASER
& PHOTONICS
REVIEWS

www.lpr-journal.org

Figure 2. The measured PMDs in the planes a) parallel and b) perpendicular to the laser polarization axis. c) Angular distributions determined from the measured PMDs (a,b). d) Schematic view of surface emission from an illuminated Cu nanoparticle with arrows representing the emission of the dipolar excitations.

as the laser intensity increases (0.25 eV for Figure 3b and 0.23 eV for Figure 3c). These observations indicate that the central spot and the momentum ring respond differently to the laser intensity modification. We can thus speculate that they account for two independent ionization mechanisms. We have observed three characteristic distributions: the polarization-dependent dipole distribution, the central spot, and the momentum ring. To identify the underlying mechanisms, we implement different theoretical models to reproduce these characteristic distributions. We first perform the calculations for the dipole photoemission based on the surface multiphoton emission model.[38] This model presents a comprehensive treatment of weak-field photoemission from metal surfaces, including surface effects such as electron reflection and backscattering. The simulated momentum distribution in **Figure 4**a exhibits an apparent dipolar enhancement effect in the direction of laser polarization. The observed agreement between experiment and theory underscores the dominant role of surface-mediated photoelectron emission in Region I. Noteworthy is the extra collection of low-energy electrons in the center (Figure 2a,b) compared to the simulated distribution. This can be attributed to the scattering from the impurities, such as residual solvent molecules, attached to the surface during sample preparation.[39] The interactions of emitted electrons with the impurities will reduce the electron energies.

Next, we discuss the appearance of the central spot and the momentum ring. Intuitively the ring structure stems from multiphoton emission, verified by the above-threshold ionization peaks of the photoelectron energy spectrum (see the Supporting Information). Moreover, the photoelectrons forming the mo-

mentum ring can be identified to originate from the volume instead of the surface due to the isotropic structure. Thus we implement the Monte Carlo method within the ballistic volume multiphoton emission model[40,41] to reproduce the measured momentum ring. This model accounts for the excitation, ballistic traveling, and transmission into the vacuum of emitted volume photoelectrons. Figure 4b shows the calculated distribution of volume-emitting photoelectrons, which does exhibit an isotropic ring structure consistent with the experimental observation. As for the isotropic central spot exhibiting a smooth decay from the center to the surroundings, it is the typical distribution of thermionic emission. To clarify the role of thermionic emission, electron temperatures are calculated for CuNPs under femtosecond pulsed excitation utilizing the two-temperature model.[42] In this model, the electron gas thermalizes via electron–electron scattering due to the decay of excited plasmons into electron–hole pairs. The final thermionic current is calculated via the Richardson–Dushman equations.[43] As shown in Figure 3c, the low-energy electrons converge to form a bright spot, which matches with the central spot in Figure 3a–c. Consequently, the experimental results in Figure 3c can be exactly regarded as a combination of the central spot (Figure 4c) and momentum ring (Figure 4b). The photoemission process in Region II is mediated by both volume and thermal emission mechanisms.

The above intensity-dependent PMDs exhibit the transition of the dominant emission mechanism from surface to volume. This transition can be attributed to the difference in strength between surface and internal plasmonic fields. According to the simulated plasmonic field distribution (see the
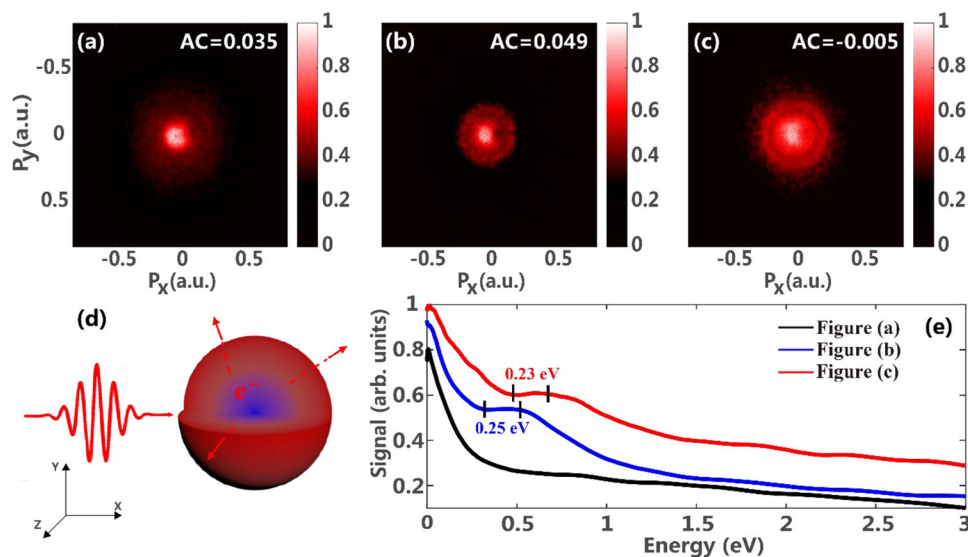
Figure 3. a–c) Representative PMDs for increasing (from left to right) laser intensity. The "hole structure," slight depression in electron yields, at the center of the PMDs are due to the degraded responsivity of our detector. d) Schematic view of volume emission from an illuminated Cu nanoparticle (with a quarter section removed to show the volume excitation). e) The photoelectron energy spectra obtained from (a–c). The energy gap between the edge of the spot and the momentum ring is marked at corresponding curves.
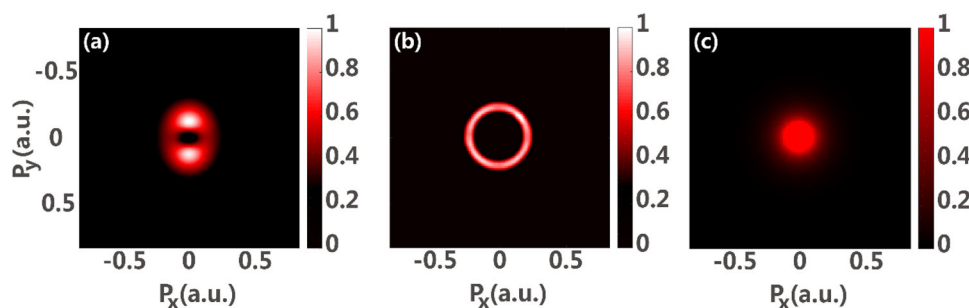

Figure 4. The simulated PMDs with the laser polarized along the y-axis calculated via a) the surface multiphoton emission model, b) the ballistic volume multiphoton emission model, and c) the Richardson–Dushman equations.

Supporting Information), the field enhancement factor at the surface is about 3.5 at maximum, while only 0.25 within the volume. Thus the surface electrons can be optically excited at lower laser intensity. However, the number of so-called "surface electrons" is much smaller considering the shallow skin depth ($\approx$3.4 nm) of CuNPs.[44] As the laser intensity increases, the volume-emitting photoelectrons gradually increase in number while surface-emitting photoelectrons reach saturation. Hence the volume emission finally dominates Region II. Besides the field strength, the spatial distribution of the field on the surface is also different from that in the body. The enhanced absorption of the metal leads to an enhanced internal electric field inside the CuNPs in the forward direction (the side illuminated by light) of the propagating laser pulses (see Supporting Information). This forward–backward asymmetry directly maps to the momentum distribution of the released ions.[45,46] However, we find that the volume-mediated photoelectrons remain isotropic even in an asymmetric volume field. This is due to the extensive electron–electron and electron-ion interaction within the volume eliminating the field asymmetry signatures.

Besides the unexpected isotropy, it is also found that the momentum ring shifts toward higher energies with the increase of laser intensity in Figure 3. This phenomenon has escaped observation in previous studies, since the laser can only work with intensity below the damage threshold of metallic materials. Meanwhile, the energy of the momentum ring shifts rather slowly as laser intensity increases in Figure 3. Thus observing this shift requires the laser intensity to vary over a wide range. Benefiting from the ADL system,[47] the damaged sample can be replaced by new ones for the next laser pulse in our experiments. So we can employ higher laser intensity than in previous studies. To investigate this response of the momentum ring to the increasing laser intensity, we introduce the intensity-dependent effects into the volume emission model. In this model, the laser intensity affects the emission process in two aspects: ponderomotive energy and electronic temperature. Theoretical calculations show that the influence of the ponderomotive energy is negligible in intensity Region II (see the Supporting Information). The momentum ring will only shift toward higher energy as the electronic temperature increases. This can be attributed to the effect of temperature on
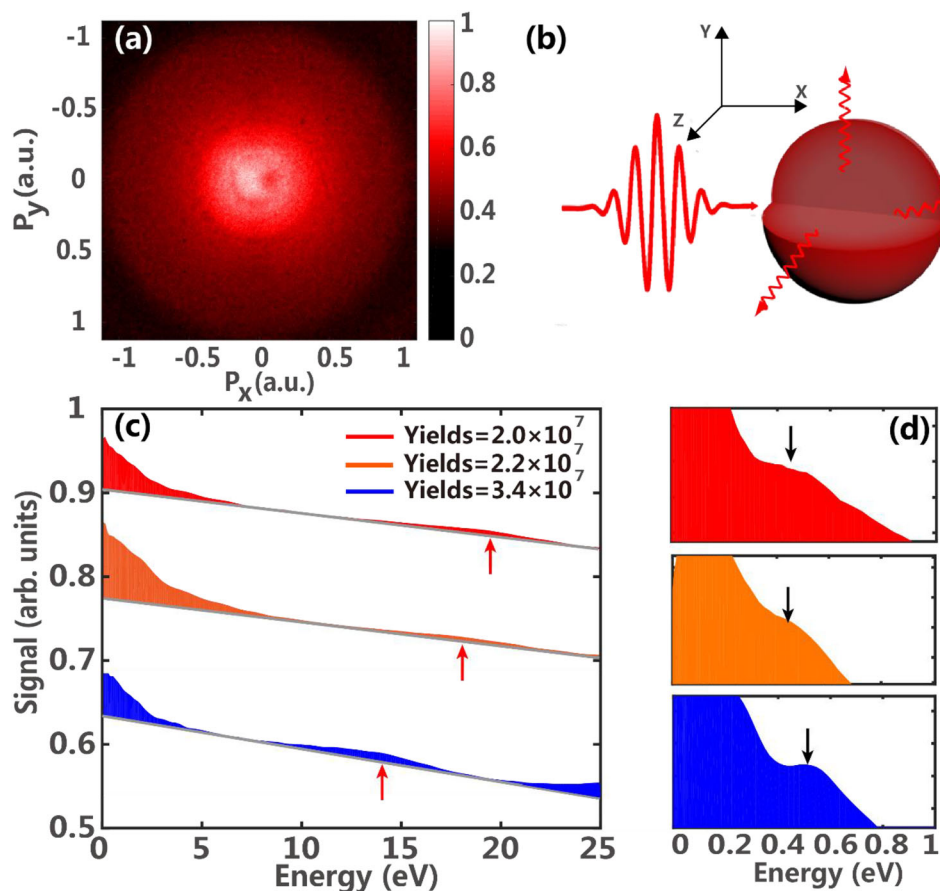
ADVANCED
SCIENCE NEWS

www.advancedsciencenews.com

LASER
& PHOTONICS
REVIEWS

www.lpr-journal.org

Figure 5. a) The measured PMDs significantly above the damage threshold at the laser intensity. b) Schematic view of thermal emission from a metal nanoplasma. c) Angle-integrated kinetic energy spectra for three different intensities. The red arrows suggest the CED characteristic peaks. d) The electron energy spectra below 1 eV of (c). The black arrows suggest the momentum rings.

the initial electron velocity distribution. According to the metal electron gas model, the increase in temperature will improve the proportion of high-energy electrons, leading to the shift of the momentum ring. This provides an efficient way to control the energy of the volume-emitting electrons.

In addition to the momentum ring, the central spot also expands as laser intensity increases. Furthermore, the gap between them keeps decreasing due to the faster expansion of the central spot, as shown in Figure 3e. One can expect that the momentum ring will be obscured by the central spot above certain laser intensity. To verify this expectation, we further increase the laser intensity into Region III. **Figure 5**a shows a typical PMD at the highest laser intensity in our experiments. The expanded central spot dominates the momentum spectrum as expected. The ring structure is almost indistinguishable in the PMD and only can be located in the energy spectra as indicated by black arrows in Figure 5d. Moreover, a new and unexpected peak is observed for each energy spectrum, as indicated by a red arrow in Figure 5c. And the peak gradually shifts toward lower energies with increasing laser intensity. Particularly the peak with the lowest energy locates at ≈ 14 eV near the binding energy, which is the sum of the work function (≈ 5 eV) and the Fermi energy (≈ 7 eV).[18,48] This extraordinary peak and its shifting are the typical signatures of

CED.[49] This electron-correlation-driven energy transfer process marks the generation of the complete plasma, and plays a significant role in nanoscale systems interacting with intense laser pulses. The peak assigned to CED suggests the transition from nanoplasmonic to complete nanoplasma state. Our experimental results also demonstrate that CED can be observed in metal-laser interaction. However, the measured CED peaks of the CuNP nanoplasma exhibit two abnormalities compared to that in gas clusters. First, the energy of the CED peaks is slightly higher than the binding energy. Second, with the enhancement of laser intensity, the CED peaks of the CuNPs do not broaden and fade as the clusters do, in which the emitted electrons lose energy that is transferred to surrounding particles by Coulomb interactions. The abnormalities can be attributed to the space charge effect on the metal surface.[50,51] The velocity of emitted electrons from metal nanoparticles follows the Maxwell–Boltzmann distribution. The Coulomb interaction between slow electrons and fast electrons will accelerate the fast electrons (see the Supporting Information). The number of atoms reaches up to 4.4×10^7 in a CuNP within a diameter of 100 nm. Compared to the gas clusters, the atom and electron density of CuNPs is significantly higher. The repulsive electric field generated within the emitted electrons is thus extraordinarily strong, leading to the CED peaks

above the binding energy. Furthermore, the space charge effect counteracts the energy loss of fast electrons so that the CED peaks are not broadened.

3. Conclusion

In conclusion, we experimentally investigate the nanoplasmon-nanoplasma transition in CuNPs with the combined ADL and VMI spectrometer. By distinguishing the characteristic PMDs with yield across six orders of magnitude, we identify the underlying emission mechanisms during the transition. Plasmonic surface-multiphoton emission initially takes a leading role, which is subsequently replaced when the transition starts. The competition of volume multiphoton and thermionic emission plays the transition state dominating the transition process. The transition is finally completed with the domination of thermionic emission. Besides, we observe CED peaks from CuNPs located where the energy is greater than the binding energy, and shifting without fading as the laser intensity increase. To the best of our knowledge, these multi-body correlated effects have not been reported before in nanoplasma formed from the metal nanoparticle. We can achieve these results over a wide range of laser intensities, most likely owing to the space charge effect caused by the repulsive field from high-density electrons.

Our work provides new insight into the formation of nanoplasma states. The transition state we demonstrate is delicate: the thermionic emission represents plasma formation, and the volume emission indicates the nanoparticle is still in a solid state. This is helpful in accurately controlling the state of nanoparticles in cancer treatment, thereby avoiding the toxicity issues induced by destruction. In addition, our work demonstrates the photoemission characteristics at each stage during the transition process. It provides a potential opportunity to further optimize the performance of nanoplasma devices, such as the time response of the nanoplasma switch.

4. Experimental Section

In the experiment, a VMI spectrometer[52] is used to measure the photoelectron momentum distributions emitted by Cu nanoparticles, as shown in **Figure 6**. A nanoplasmon or nanoplasma was formed via the illumination of a CuNP with a tightly focused linear polarized laser pulse ($\approx$35 fs, 800 nm). The laser pulse used in these experiments are generated from a Ti:Sapphire femtosecond laser system with a repetition rate of 1 kHz. The combination of a λ/2 plate of 800 nm and a broadband wire grid polarizer was used to control the laser intensity. The ADL system provided highly collimated and tightly focused particle beams, which could refresh the target for each laser pulse. The isolated Cu nanoparticles (Shanghai Chaowei Nanotechnology Co. Ltd.) dispersed in water (0.5 g L^{-1}) were aerosolized by using a commercial atomizer (TSI model 3076) to generate a nanoparticle aerosol. The Cu nanoparticles beam aerosolized using a fast carbon dioxide gas stream was focused spot size of 0.5 mm in diameter in the center of the reacting region, where ultra-high vacuum (10^{-9} mbar) conditions were maintained. Electrons derived from the reacting region were accelerated within an electrostatic field and recorded on a micro-channel plate/phosphor screen detector. The final signal would be imaged via a charge coupled device camera running at an average of 250 frames per second to match the hit rate and promise a high signal-to-noise ratio.
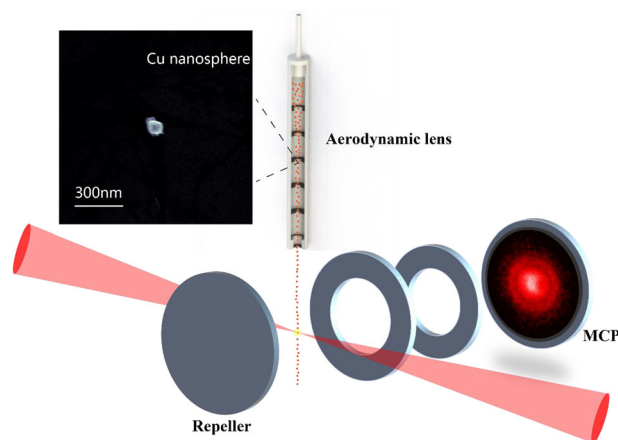

Figure 6. Schematic diagram of ADL system and VMI spectrometer of the electron emission from Cu nanoparticles in ultrafast laser fields at 800 nm. The VMI spectrometer consists of ion optics (repeller, extractor, ground plate) and an MCP screen detector. The inset shows the scanning electron micrographs of an aerosolized Cu nanoparticle used in our experiments.

Supporting Information

Supporting Information is available from the Wiley Online Library or from the author.

Conflict of Interest

The authors declare no conflict of interest.

Data Availability Statement

The data that support the findings of this study are available from the corresponding author upon reasonable request.

[1] G. Manfredi, *Phys. Plasmas* **2018**, *25*, 031701.

[2] E. Cortes, W. Xie, J. Cambiasso, A. S. Jermyn, R. Sundararaman, P. Narang, S. Schlucker, S. A. Maier, *Nat. Commun.* **2017**, *8*, 14880.

[3] J. Gargiulo, R. Berté, Y. Li, S. A. Maier, E. Cortés, *Acc. Chem. Res.* **2019**, *52*, 2525.

[4] C. Hrelescu, T. K. Sau, A. L. Rogach, F. Jäckel, G. Laurent, L. Douillard, F. Charra, *Nano Lett.* **2011**, *11*, 402.

[5] R. Hörlein, S. Steinke, A. Henig, S. Rykovanov, M. Schnürer, T. Sokollik, D. Kiefer, D. Jung, X. Yan, T. Tajima, J. Schreiber, M. Hegelich, P. Nickles, M. Zepf, G. Tsakiris, W. Sandner, D. Habs, *Laser Part. Beams* **2011**, *29*, 383.

[6] D. D. Hickstein, F. Dollar, J. A. Gaffney, M. E. Foord, G. M. Petrov, *Phys. Rev. Lett.* **2013**, *112*, 313.

[7] G. Cristoforetti, A. Anzalone, F. Baffigi, G. Bussolino, G. D'Arrigo, L. Fulgentini, A. Giulietti, P. Koester, L. Labate, S. Tudisco, *Plasma Phys. Controlled Fusion* **2014**, *56*, 095001.

[8] K. Ostrikov, F. Beg, A. Ng, *Rev. Mod. Phys.* **2016**, *88*, 011001.

[9] K. Ostrikov, E. C. Neyts, M. Meyyappan, *Adv. Phys.* **2013**, *62*, 113.

[10] X. Zhang, X. Li, D. Zhang, N. Q. Su, W. Yang, H. O. Everitt, J. Liu, *Nat. Commun.* **2017**, *8*, 14542.

[11] E. Cortés, *Adv. Opt. Mater.* **2017**, *5*, 1700191.

[12] U. Aslam, V. G. Rao, S. Chavez, S. Linic, *Nat. Catal.* **2018**, *1*, 656.

[13] M. Graf, D. Jalas, J. Weissmuller, A. Y. Petrov, M. Eich, *ACS Catal.* **2019**, *9*, 3366.

[14] C. Clavero, *Nat. Photonics* **2014**, *8*, 95.

[15] K. Wu, J. Chen, J. R. McBride, T. Lian, *Science* **2015**, *349*, 632.

[16] M. W. Knight, H. Sobhani, P. Nordlander, N. J. Halas, *Science* **2011**, *332*, 702.

[17] M. L. Brongersma, N. J. Halas, P. Nordlander, *Nat. Nanotechnol.* **2015**, *10*, 25.

[18] J. Pettine, P. Choo, F. Medeghini, T. W. Odom, D. J. Nesbitt, *Nat. Commun.* **2020**, *11*, 1367.

[19] R. G. Hobbs, W. P. Putnam, A. Fallahi, Y. Yang, F. X. Kärtner, K. K. Berggren, *Nano Lett.* **2017**, *17*, 6069.

[20] X. Xiong, Y. Zhou, Y. Luo, X. Li, M. Bosman, L. K. Ang, P. Zhang, L. Wu, *ACS Nano* **2020**, *14*, 8806.

[21] C. Karnetzky, P. Zimmermann, C. Trummer, C. D. Sierra, M. Wörle, R. Kienberger, A. Holleitner, *Nat. Commun.* **2018**, *9*, 2471.

[22] M. Müller, A. Paarmann, R. Ernstorfer, *Nat. Commun.* **2014**, *5*, 5292.

[23] E. Lukianova-Hleb, E. Hanna, J. Hafner, D. Lapotko, *Nanotechnology* **2010**, *21*, 085102.

[24] D. Wagner, N. Delk, E. Lukianova-Hleb, J. Hafner, M. Farach-Carson, D. Lapotko, *Biomaterials* **2010**, *31*, 7567.

[25] L. Anderson, E. Hansen, E. Lukianova-Hleb, J. Hafner, D. Lapotko, *J. Controlled Release* **2010**, *144*, 151.

[26] E. Y. Lukianova-Hleb, A. P. Samaniego, J. Wen, L. S. Metelitsa, C. Chang, D. Lapotko, *J. Controlled Release* **2011**, *152*, 286.

[27] D. Lapotko, *Cancers* **2011**, *3*, 802.

[28] E. Y. Lukianova-Hleb, A. Belyanin, S. Kashinath, X. Wu, D. O. Lapotko, *Biomaterials* **2012**, *33*, 1821.

[29] J. Baumgart, L. Humbert, E. Boulais, R. Lachaine, J. Lebrun, M. Meunier, *Biomaterials* **2012**, *33*, 2345.

[30] E. Boulais, R. Lachaine, M. Meunier, *Nano Lett.* **2012**, *12*, 4763.

[31] R. Lachaine, E. Boulais, M. Meunier, *ACS Photonics* **2014**, *1*, 331.

[32] M. S. Nikoo, A. Jafari, N. Perera, M. Zhu, G. Santoruvo, E. Matioli, *Nature* **2020**, *579*, 534.

[33] L. Ban, B. L. Yoder, R. Signorell, *Annu Rev Phys Chem* **2020**, *71*, 315.

[34] Y. Luo, Y. Zhou, P. Zhang, *Phys. Rev. B* **2021**, *103*, 085410.

[35] Y. Zhou, P. Zhang, *J. Appl. Phys.* **2021**, *130*, 064902.

[36] F. Süßmann, S. Zherebtsov, J. Plenge, N. G. Johnson, M. Kübel1, A. M. Sayler, V. Mondes, C. Graf, E. Rühl, G. G. Paulus, D. Schmischke, P. Swrschek, M. F. Kling, *Rev. Sci. Instrum.* **2011**, *82*, 093109.

[37] F. Süßmann, S. L. Seiffert, S. Zherebtsov, V. Mondes, J. Stierle, M. Arbeiter, J. Plenge, P. Rupp, C. Peltz, A. Kessel, S. A. Trushin, B. Ahn, D. Kim, C. Graf, E. Rühl, M. F. Kling, T. Fennel, *Nat. Commun.* **2015**, *6*, 7944.

[38] S. V. Yalunin, M. Gulde, C. Ropers, *Phys. Rev. B* **2011**, *84*, 195426.

[39] J. Pettine, A. Grubisic, D. J. Nesbitt, *J. Phys. Chem. C* **2018**, *122*, 3970.

[40] J. Pettine, A. M. Menendez, D. J. Nesbitt, *J. Chem. Phys.* **2020**, *153*, 101101.

[41] J. Pettine, S. M. Meyer, F. Medeghini, C. J. Murphy, D. J. Nesbitt, *ACS Nano* **2021**, *15*, 1566.

[42] G. V. Hartland, *Chem. Rev.* **2011**, *111*, 3858.

[43] N. W. Ashcroft, N. D. Mermin, Solid State Physics, Saunders College, Philadelphia **1976**.

[44] E. D. Palik, *Handbook of Optical Constants of Solids*, Academic Press, New York **1998**.

[45] E. Antonsson, F. Gerke, L. Merkel, I. Halfpap, B. Langer, E. Rühl, *Phys. Chem. Chem. Phys.* **2019**, *21*, 12130.

[46] D. D. Hickstein, F. Dollar, J. L. Ellis, K. J. Schnitzenbaumer, K. E. Keister, G. M. Petrov, C. Ding, B. B. Palm, J. A. Gaffney, M. E. Foord, S. B. Libby, G. Dukovic, J. L. Jimenez, H. C. Kapteyn, M. M. Murnane, W. Xiong, *ACS Nano* **2014**, *8*, 8810.

[47] P. S. K. Liu, R. Deng, K. A. Smith, L. R. Williams, J. T. Jayne, M. R. Canagaratna, K. Moore, T. B. Onasch, D. R. Worsnop, T. Deshler, *Aerosol Sci. Technol.* **2007**, *41*, 721.

[48] S. Li, S. Li, F. Zhang, D. Tian, H. Li, D. Liu, Y. Jiang, A. Chen, M. Jin, *Appl. Surf. Sci.* **2015**, *355*, 681.

[49] B. Schütte, M. Arbeiter, T. Fennel, G. Jabbari, A. I. Kuleff, M. J. J. Vrakking, A. Rouzée, *Nat. Commun.* **2015**, *6*, 8596.

[50] S. Hellmann, K. Rossnagel, M. Marczynski-Bühlow, L. Kipp, *Phys. Rev. B* **2009**, *79*, 035402.

[51] W. Hu, Y. C. Shin, G. King, *Phys. Plasmas* **2011**, *18*, 093302.

[52] A. T. J. B. Eppink, D. H. Parker, *Rev. Sci. Instrum.* **1998**, *68*, 3477.